

RESEARCH ARTICLE | JULY 23 2025

PIAFS: A 2D nonlinear hydrodynamics code to model gaseous optics

Special Collection: [Progress in Inertial Fusion Energy Research: Two Years After Ignition](#)

A. Oudin  ; D. Ghosh  ; C. Riconda  ; L. Lancia  ; E. Kur  ; K. Ou  ; V. M. Perez-Ramirez  ; J. Lee  ; M. R. Edwards  ; P. Michel



Phys. Plasmas 32, 072714 (2025)

<https://doi.org/10.1063/5.0268318>



Articles You May Be Interested In

Large-amplitude density waves produced in ozone-mixed gas by ultraviolet laser irradiation

Physics of Fluids (April 2024)

Overstability of acoustic waves in heat-releasing gaseous media

AIP Conf. Proc. (December 2020)

Saturation of multi-laser beams laser-plasma instabilities from stochastic ion heating

Phys. Plasmas (April 2013)

PIAFS: A 2D nonlinear hydrodynamics code to model gaseous optics

Cite as: Phys. Plasmas **32**, 072714 (2025); doi: [10.1063/5.0268318](https://doi.org/10.1063/5.0268318)

Submitted: 28 February 2025 · Accepted: 7 July 2025 ·

Published Online: 23 July 2025



View Online



Export Citation



CrossMark

A. Oudin,^{1,a)} D. Ghosh,¹ C. Riconda,² L. Lancia,³ E. Kur,⁴ K. Ou,⁴ V. M. Perez-Ramirez,⁴ J. Lee,⁴ M. R. Edwards,⁴ and P. Michel¹

AFFILIATIONS

¹Lawrence Livermore National Laboratory, Livermore, California 94551, USA

²LULI, Sorbonne Université, CNRS, Ecole Polytechnique, CEA, F-75252 Paris, France

³LULI, CNRS, CEA, Sorbonne Université, Ecole Polytechnique, Institut Polytechnique de Paris, F-91128 Palaiseau, France

⁴Stanford University, Stanford, California 94305, USA

Note: This paper is part of the Special Topic on Progress in Inertial Fusion Energy Research: Two Years After Ignition.

a) Author to whom correspondence should be addressed: oudin1@llnl.gov

ABSTRACT

The survivability of final optics is expected to be a major challenge for all future inertial fusion energy concepts. Due to their higher damage threshold, gaseous optics have been identified as a promising solution to this problem. Gaseous optics can be created through the photoabsorption of spatially modulated UV light, which induces various chemical processes that heat the gas. This heating leads to a pressure perturbation, which in turn launches a density perturbation that can imprint a refractive index modulation such as a grating. In this article, we introduce a parallel C/C++ code to simulate gaseous optics. PIAFS2D is a high-order conservative finite-difference code to solve the compressible Navier–Stokes equations along with the photochemical heating sources on Cartesian grids. The simulations are validated by the linear theory derived in a previous paper [Michel *et al.*, Phys. Rev. Appl. **22**, 024014 (2024)]. For larger perturbations, the behavior of the system—particularly the evolution of the generated acoustic wave—demonstrates strong nonlinearity. PIAFS2D allows the study of nonlinear behaviors and can be used for the design of high-efficiency gaseous optics elements in realistic experimental conditions.

© 2025 Author(s). All article content, except where otherwise noted, is licensed under a Creative Commons Attribution (CC BY) license (<https://creativecommons.org/licenses/by/4.0/>). <https://doi.org/10.1063/5.0268318>

23 September 2025 / 18:45:04

I. INTRODUCTION

Inertial Fusion Energy (IFE)¹ aims to generate clean and sustainable energy through laser-driven nuclear fusion. Since ignition has been reached at the National Ignition Facility (NIF),^{2,3} research on IFE has received much interest. Several approaches are being considered, all of them involving the transport of high-energy laser beams to fusion targets injected at a high repetition rate (~ 10 Hz) inside a target chamber. Therefore, a common challenge for all the future facilities is to develop “final optics”—the last optical elements before the target, and therefore in its direct line of sight—that can sustain the extreme environment of an IFE facility (neutron and x-ray flux, debris, and, to lesser degree, the fluence of the drive laser itself).

Research on optical materials meeting the extreme requirements of final optics in IFE has been limited. One proposed option is liquid metal reflectors,⁴ although combined tests of survivability and optical quality have never been performed. Plasma optics have been studied as a promising candidate to replace solid-state optical elements by

shaping the refractive index sustained by the free electrons.^{5,6} However, plasma optics have short lifetimes (up to tens of ps), which make them better suited to short-pulse, high-intensity laser applications than IFE, where pulse durations are typically nanosecond-scale.

A promising solution is to use gaseous optics, where a diffractive pattern has been imprinted in the gas using localized absorption of a low-energy “imprint” laser beam. The concept was recently demonstrated in a proof-of-principle experiment^{7,8} and investigated theoretically.⁹ Because gas optics are transient, they do not suffer from debris or neutron damage, and furthermore, they can sustain laser fluences of kJ cm^{-2} without optical damage. Figure 1 shows how a gas mirror would be used in an IFE target chamber.

In this concept, two UV beams overlap in a neutral gas, here a mixture of ozone (O_3) and oxygen (O_2). At the locations of the bright interference fringes, the absorption of UV photons by O_3 molecules leads to the photodissociation of O_3 into O_2 and O , usually in some excited states. This main reaction is exothermic and responsible for

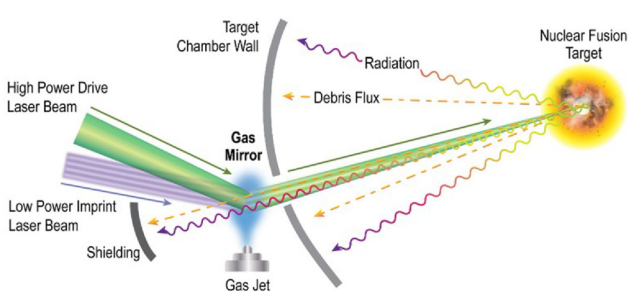


FIG. 1. Illustration of a gas mirror used as a final optic at the entrance of an IFE target chamber wall. The spatially modulated low-power imprint beam creates a density modulation in a gas jet, turning the gas into a diffraction grating that can safely direct the high-power drive laser beam toward the fusion target.

most of the gas heating. Other secondary processes result from the reaction between O₂ and O in their excited states and the background gas. The chemical reactions are the same as those involved in the ozone cycle in the upper atmosphere and are therefore well known and documented.^{10,11} The heating of the gas creates pressure and entropy perturbations, which, respectively, launch a standing acoustic wave and an entropy mode (isobaric, non-propagating modulation of entropy), leading to a density modulation. In a previous work,⁹ a theory of the linear evolution of the acoustic/entropy wave induced by the chemical heating induced by two lasers crossing at an angle was derived. It showed a good qualitative agreement with the aforementioned experiment.⁷ However, at high fluence/ozone density, the hydrodynamic evolution is expected to go beyond the limits of validity of the linear theory.

In this work, we develop PIAFS2D, a hydrodynamic code that combines the coupled evolution of the chemistry and nonlinear hydrodynamics. PIAFS stands for Photochemically Induced Acousto-optics Fluid Simulations. The code is based on a conservative high-order finite-difference numerical model for the 2D Navier-Stokes equations on a Cartesian grid. The spatial derivatives for the convective and acoustic terms are computed using the fifth-order upwind weighted essentially nonoscillatory (WENO)¹² scheme, while the viscous and thermal conduction terms are discretized with fourth-order central finite differences. The classical fourth-order, four-stage Runge-Kutta (RK4) scheme is used to evolve the equations in time.

The paper is organized as follows: in Sec. II, we describe PIAFS2D, including the governing equations and its numerical discretization. In Sec. III, we compare the simulation results to linear theory. First, we validate the results of our previous work.⁹ Then, we describe the physics of the nonlinearity and how PIAFS captures it. Section IV concludes our work and discusses prospects for future investigations.

II. NUMERICAL METHOD

A. Governing equations

The governing equations are the normalized two-dimensional Navier-Stokes equations¹⁵ with a chemical heating source term

$$\partial_t \mathbf{U} + \partial_x \mathbf{F} + \partial_y \mathbf{G} = \partial_x \mathbf{F}_v + \partial_y \mathbf{G}_v + \mathbf{S}, \quad (1)$$

where $\partial_{x,y,t}$ represent derivatives with respect to x , y , and t , respectively, and \mathbf{U} is the state variable

$$\mathbf{U} = [\rho, \rho u, \rho v, E]^T.$$

The convective fluxes, $\mathbf{F} \equiv \mathbf{F}(\mathbf{U})$ and $\mathbf{G} \equiv \mathbf{G}(\mathbf{U})$, are

$$\mathbf{F} = [\rho u, \rho u^2 + P, \rho uv, (E + P)u]^T,$$

$$\mathbf{G} = [\rho v, \rho uv, \rho v^2 + P, (E + P)v]^T,$$

and the dissipative (viscous and conduction) fluxes are

$$\mathbf{F}_v = [0, \tau_{xx}, \tau_{xy}, u\tau_{xx} + v\tau_{xy} - q_x]^T,$$

$$\mathbf{G}_v = [0, \tau_{yx}, \tau_{yy}, u\tau_{yx} + v\tau_{yy} - q_y]^T.$$

The chemical heating source term is

$$\mathbf{S} = [0, 0, 0, Q_c/(\gamma - 1)]^T.$$

The fluid density is ρ . The Cartesian velocity components along x and y are u and v , respectively, and P is the pressure. The internal energy and the temperature are given by

$$E = \frac{P}{\gamma - 1} + \frac{1}{2}\rho(u^2 + v^2), \quad T = \frac{\gamma P}{\rho}, \quad (2)$$

where γ is the specific heat ratio. The viscous and the heat conduction terms in Eq. (1) are given by

$$\tau_{xx} = \frac{2\mu}{3Re}(2\partial_x u - \partial_y v), \quad (3a)$$

$$\tau_{xy} = \tau_{yx} = \frac{\mu}{Re}(\partial_y u + \partial_x v), \quad (3b)$$

$$\tau_{yy} = \frac{2\mu}{3Re}(-\partial_x u + 2\partial_y v), \quad (3c)$$

$$q_{x,y} = \frac{1}{(\gamma - 1)PrRe}\kappa\partial_{x,y}T. \quad (3d)$$

Here, Re and Pr are the Reynolds and Prandtl numbers, respectively, defined as

$$Re = \frac{\rho_{ref}c_{ref}x_{ref}}{\mu_{ref}}, \quad Pr = \frac{c_p\mu_{ref}}{\kappa_{ref}},$$

where the subscript $(\cdot)_{ref}$ denotes reference quantities used to normalize (1), μ and κ are the coefficients of viscosity and thermal conductivity, respectively, c denotes the speed of sound, and $c_p = 918.45 \text{ J kg}^{-1} \text{ K}^{-1}$ is the specific heat capacity of oxygen (O₂) at 288 K. The gas constant is

$$R = \frac{N_A k_B}{M_{O_2}} \approx 259.7 \text{ J kg}^{-1} \text{ K}^{-1},$$

where N_A is the Avogadro number, k_B is the Boltzmann constant, and M_{O_2} is the molar mass of oxygen. The reference length for the simulations reported in this paper is determined by the physical setup shown in Fig. 2

$$x_{ref} = \frac{\lambda_{UV}}{4\pi \sin \theta} = 6.65 \times 10^{-6} \text{ m} = 6.65 \mu\text{m}, \quad (4)$$

where $\lambda_{UV} = 248 \text{ nm}$ is the pump wavelength, and $\theta = 0.17^\circ$ is the half-crossing angle between the two UV pumps. The remaining reference quantities for our simulations are:¹⁶

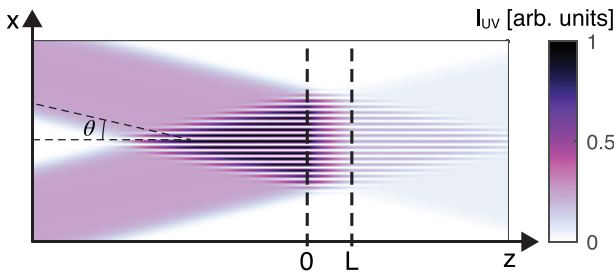


FIG. 2. Two UV beams crossing at a half-angle θ create an interference pattern of wavelength $\lambda_g = \lambda_{UV}/[2 \sin \theta]$ inside a volume of gas containing a small fraction of ozone located between $z = 0$ and $z = L$. The absorption of UV light heats the gas in the constructive interference regions and imprints a diffraction grating of wavelength λ_g .

$$\begin{aligned} T_{ref} &= 288 \text{ K}, \quad \rho_{ref} = \frac{P_{tot}}{RT_{ref}} = 1.356 \text{ kg m}^{-3}, \\ \mu_{ref} &= \mu_{O_2}(T_{ref}) = 1.99 \times 10^{-5} \text{ kg s}^{-1} \text{ m}^{-1}, \\ \kappa_{ref} &= \kappa_{O_2}(T_{ref}) = 2.70 \times 10^{-2} \text{ W m}^{-1} \text{ K}^{-1}, \\ c_{ref} &= \sqrt{\gamma R T_{ref}} = 323.59 \text{ ms}^{-1}, \\ t_{ref} &= \frac{x_{ref}}{c_{ref}} = 2.06 \times 10^{-8} \text{ s} = 20.6 \text{ ns}, \quad P_{ref} = \rho_{ref} c_{ref}^2. \end{aligned}$$

Consequently, the Reynolds and Prandtl numbers for our simulations are

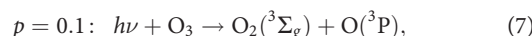
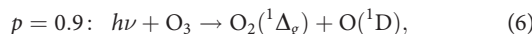
$$Re \approx 147, \quad Pr \approx 0.68.$$

The normalized coefficients of viscosity and thermal conductivity are computed as

$$\mu = \frac{\tilde{T}^{3/2}}{T_0} \left(\frac{T_0 + T_S}{\tilde{T} + T_S} \right), \quad \kappa = \frac{\tilde{T}^{3/2}}{T_0} \left(\frac{T_0 + T_A e^{-T_B/T_0}}{\tilde{T} + T_A e^{-T_B/T}} \right), \quad (5)$$

where $\tilde{T} = T T_{ref}$ is the physical temperature (in Kelvin), $T_0 = 275 \text{ K}$, $T_S = 110.4 \text{ K}$, $T_A = 245.4 \text{ K}$, and $T_B = 27.6 \text{ K}$.

In addition to the hydrodynamic equations, we solve the reaction equations that govern the evolution of the local concentration of the reacting species. The absorption of UV light by ozone within the Hartley band ($\lambda \in [200-300] \text{ nm}$) is observed in the atmosphere and thus has been extensively studied. All subsequent chemical reactions are therefore well documented.¹⁷ The first and main reaction is the absorption of a photon by an ozone molecule, leading to its photodissociation, following two different channels with different probabilities p :



where $h\nu$ is the energy carried by a photon. This photodissociation produces oxygen atoms and molecules in excited states that will react with the background and produce new reactions, of which we include

$$\begin{aligned} \frac{d}{dt}[O_3] &= -(k_{0a} + k_{0b})[h\nu][O_3] - (k_{2a} + k_{2b})[^1D][O_3] \\ &\quad - (k_{3a} + k_{3b})[^1\Sigma_g][O_3], \end{aligned} \quad (8a)$$

$$\begin{aligned} \frac{d}{dt}[^1D] &= k_{0a}[h\nu][O_3] - (k_{1a} + k_{1b})[^1D][O_2] \\ &\quad - (k_{2a} + k_{2b})[^1D][O_3], \end{aligned} \quad (8b)$$

$$\frac{d}{dt}[^1\Delta_g] = k_{0a}[h\nu][O_3] + k_{1b}[O_2][^1D], \quad (8c)$$

$$\begin{aligned} \frac{d}{dt}[^1\Sigma_g] &= k_{1a}[^1D][O_2], \\ &\quad - (k_{3a} + k_{3b})[^1\Sigma_g][O_3], \end{aligned} \quad (8d)$$

where square brackets represent concentrations in cm^{-3} , ${}^1\Delta_g$, ${}^1\Sigma_g$, and 1D are molecular quantum states with electronic energies of 1, 1.6, and 2 eV, respectively, and k_i are the reaction rates of reaction i (cf. Table I). The evolution of the photon concentration, $[h\nu]$, is given by

$$\frac{d}{dz}[h\nu] = \sigma[h\nu][O_3], \quad (9)$$

where σ is the absorption cross section of ozone. The chemical heating term in Eq. (1) is calculated by solving the concentration of molecules (and UV photons) vs (x, y, z, t) from coupled rate equations [Eq. (8)] as

$$\begin{aligned} Q_c &= (q_{0a}k_{0a} + q_{0b}k_{0b})[h\nu][O_3] \\ &\quad + (q_{1a}k_{1a} + q_{1b}k_{1b})[^1D][O_2] \\ &\quad + (q_{2a}k_{2a} + q_{2b}k_{2b})[^1D][O_3], \end{aligned} \quad (10)$$

where q_i represents the heat energy normalized to the initial internal energy of the reaction i in Table I: $q_i = E_{heat,i}/E_{init}$ where the initial internal energy is $E_{init} = P_{gas}/(\gamma - 1)[O_2]$. More details on the chemical reactions can be found in Ref. 9.

B. Numerical discretization

Equation (1) is discretized on a two-dimensional Cartesian grid with $\{i, j\}$ as the grid index. We use the conservative finite-difference formulation^{12,18,19} for the spatial derivative terms on the left-hand side (LHS), $\partial_x \mathbf{F}$ and $\partial_y \mathbf{G}$. Since these terms represent nonlinear convective and acoustic waves, they are discretized using a characteristic-based upwind scheme¹² to avoid numerical oscillations across shocks and strong gradients. The discretization is implemented independently along each dimension; the following describes the discretization of $\partial_x \mathbf{F}$ and can be trivially extended to the computation of $\partial_y \mathbf{G}$. The index j is omitted for convenience of notation. The conservative finite-difference approximation for the x -derivative at a grid cell i is

$$\left. \frac{\partial \mathbf{F}}{\partial x} \right|_i = \frac{1}{\Delta x} \left[\hat{\mathbf{F}}_{i+\frac{1}{2}} - \hat{\mathbf{F}}_{i-\frac{1}{2}} \right], \quad (11)$$

where Δx is the grid spacing along x , and $\hat{\mathbf{F}}_{i\pm\frac{1}{2}}$ are the numerical approximations (of the desired order of accuracy) to the flux primitive (indefinite integral of the flux of the flux function \mathbf{F}) computed at the cell faces $i\pm\frac{1}{2}$.

The characteristic-based upwind calculation of $\hat{\mathbf{F}}_{i+\frac{1}{2}}$ is implemented as follows: First, the Roe-averaged state²⁰ at the cell face $i + \frac{1}{2}$, $\mathbf{U}_{i+\frac{1}{2}}^{\text{Roe}}$, is computed from $\mathbf{U}_{i,i+1}$, the state vector at grid cells i and $i + 1$, respectively. It is an averaged state that satisfies the following:

$$\mathbf{F}(\mathbf{U}_{i+1}) - \mathbf{F}(\mathbf{U}_i) = A \left(\mathbf{U}_{i+\frac{1}{2}}^{\text{Roe}} \right) (\mathbf{U}_{i+1} - \mathbf{U}_i), \quad (12)$$

TABLE I. Summary of all the reactions contributing to the heating of the gas over the few ns timescales relevant to gas optics. $\Delta_r H^0$ is the reaction enthalpy, and E_{heat} is the sum of translational and rotational energies of the products, which constitutes the energy available to heat the surrounding gas molecules over the relevant time scales for each reaction.

No.	Reaction	Rate (cm ³ /s)	$-\Delta_r H^0$ (eV)	E_{heat} (eV)	Reference
0a	$h\nu + O_3 \rightarrow O_2(^1\Delta_g) + O(^1D)$	$k_{0a} = 0.9 \times 3.3 \times 10^{-7}$	0.96	0.73	
0b	$h\nu + O_3 \rightarrow O_2 + O$	$k_{0b} = 0.1 \times 3.3 \times 10^{-7}$	3.95	2.8	
1a	$O(^1D) + O_2 \rightarrow O + O_2(^1\Sigma_g)$	$k_{1a} = 0.8 \times 3.95 \times 10^{-11}$	0.34	0.29	13
1b	$O(^1D) + O_2 \rightarrow O + O_2(^1\Delta_g)$	$k_{1b} = 0.2 \times 3.95 \times 10^{-11}$	0.99	0.84	13
2a	$O(^1D) + O_3 \rightarrow 2O_2$	$k_{2a} = 1.2 \times 10^{-10}$	6.0	4.3	13
2b	$O(^1D) + O_3 \rightarrow O_2 + 2O$	$k_{2b} = 1.2 \times 10^{-10}$	0.9	0.81	13
3a	$O_2(^1\Sigma_g) + O_3 \rightarrow O + 2O_2$	$k_{3a} = 1.2 \times 10^{-11}$	0.53	0.42	14
3b	$O_2(^1\Sigma_g) + O_3 \rightarrow O_3 + O_2$	$k_{3b} = 1 \times 10^{-11}$	1.63	1.16	14

where

$$A\left(\mathbf{U}_{i+\frac{1}{2}}^{Roe}\right) = \frac{d\mathbf{F}}{d\mathbf{U}} \Big|_{\mathbf{U}=\mathbf{U}_{i+\frac{1}{2}}^{Roe}} \quad (13)$$

is the flux Jacobian matrix. The eigenstructure of the $A(\mathbf{U}_{i+\frac{1}{2}}^{Roe})$ has four eigenvalues (two entropy waves and two acoustic waves), and

$$\Lambda_{i+\frac{1}{2}} \equiv A\left(\mathbf{U}_{i+\frac{1}{2}}^{Roe}\right) = \text{Diag}[u, u, u+c, u-c] \quad (14)$$

is the diagonal matrix of eigenvalues where u and c are the velocity and local speed of sound for the state $\mathbf{U}_{i+\frac{1}{2}}^{Roe}$. Let

$$L_{i+\frac{1}{2}} \equiv L\left(\mathbf{U}_{i+\frac{1}{2}}^{Roe}\right), \quad R_{i+\frac{1}{2}} \equiv R\left(\mathbf{U}_{i+\frac{1}{2}}^{Roe}\right) \quad (15)$$

denote the left and right eigenmatrices, respectively, that is to say, their rows and columns are left and right eigenvectors; consequently, they satisfy

$$R_{i+\frac{1}{2}} L_{i+\frac{1}{2}} = \mathcal{I}, \quad R_{i+\frac{1}{2}} \Lambda_{i+\frac{1}{2}} L_{i+\frac{1}{2}} = \frac{\partial \mathbf{F}}{\partial \mathbf{U}} \Big|_{\mathbf{U}=\mathbf{U}_{i+\frac{1}{2}}^{Roe}}. \quad (16)$$

We use the solution-dependent fifth-order WENO scheme¹² to interpolate the flux primitive at the cell interface ($i + \frac{1}{2}$) from the cell-centered flux values in the characteristic space. This is summarized as follows: a left-biased approximation to the k th component of the characteristic flux (i.e., the projection of the flux vector \mathbf{F} on the k th left eigenvector or the k th row of $L_{i+\frac{1}{2}}$) is computed as

$$\begin{aligned} \varphi_{i+\frac{1}{2}}^{L,(k)} &= \frac{\omega_1}{3} \varphi_{i-2}^{(k)} - \frac{1}{6} (7\omega_1 + \omega_2) \varphi_{i-1}^{(k)} \\ &+ \frac{1}{6} (11\omega_1 + 5\omega_2 + 2\omega_3) \varphi_i^{(k)} \\ &+ \frac{1}{6} (2\omega_2 + 5\omega_3) \varphi_{i+1}^{(k)} - \frac{\omega_3}{6} \varphi_{i+2}^{(k)}, \end{aligned} \quad (17)$$

where

$$\varphi_{(\dots)}^{(k)} = \mathbf{I}^{(k)} \cdot \mathbf{F}_{(\dots)} \quad (18)$$

is the k th characteristic flux, and $\mathbf{I}^{(k)}$ is the k th left eigenvector (k th row of $L_{i+\frac{1}{2}}$). We note that k is used in this subsection as an index for the eigenmodes and should not be confused with the reaction rates denoted

by $k_{(\dots)}$ in the previous Subsection II A. The coefficients $\omega_{1,2,3}$ in Eq. (17) are computed based on the local smoothness of the solution

$$\beta_1 = \frac{13}{12} \left(\varphi_{i-2}^{(k)} - 2\varphi_{i-1}^{(k)} + \varphi_i^{(k)} \right)^2 + \frac{1}{4} \left(\varphi_{i-2}^{(k)} - 4\varphi_{i-1}^{(k)} + 3\varphi_{i-2}^{(k)} \right)^2, \quad (19a)$$

$$\beta_2 = \frac{13}{12} \left(\varphi_{i-1}^{(k)} - 2\varphi_i^{(k)} + \varphi_{i+1}^{(k)} \right)^2 + \frac{1}{4} \left(\varphi_{i-1}^{(k)} - \varphi_{i+1}^{(k)} \right)^2, \quad (19b)$$

$$\beta_3 = \frac{13}{12} \left(\varphi_i^{(k)} - 2\varphi_{i+1}^{(k)} + \varphi_{i+2}^{(k)} \right)^2 + \frac{1}{4} \left(3\varphi_i^{(k)} - 4\varphi_{i+1}^{(k)} + \varphi_{i+2}^{(k)} \right)^2, \quad (19c)$$

$$\begin{aligned} \alpha_m &= \frac{c_m}{(\epsilon + \beta_m)^2}, \quad c_1 = \frac{1}{10}, \quad c_2 = \frac{3}{5}, \quad c_3 = \frac{3}{10} \\ \omega_m &= \frac{\alpha_m}{\sum_{n=1}^3 \alpha_n}, \quad m = 1, 2, 3, \quad \epsilon = 10^{-6}. \end{aligned} \quad (19d)$$

In the above equations $\beta_{1,2,3}$ are the local smoothness indicators. When the solution is smooth, $\omega_m \rightarrow c_m$, and Eq. (17) results in a fifth-order accurate interpolation.¹² However, the presence of discontinuities or sharp gradients results in one or more (but not all three) of the weights approaching zero; consequently, Eq. (17) behaves as an interpolation that is biased away from the non-smooth region and yields a nonoscillatory result. The same procedure is used to compute the right-biased approximation to the k th characteristic flux, $\varphi_{i+\frac{1}{2}}^{R,(k)}$, by reflecting all the indices in Eqs. (17) and (19) around $i + \frac{1}{2}$.

The upwind k th characteristic flux at the interface, $\varphi_{i+\frac{1}{2}}^{(k)}$, is computed from its left- and right-biased values using the Roe-fixed method:^{12,19}

$$\text{if } \lambda_i^{(k)}, \lambda_{i+\frac{1}{2}}^{(k)}, \lambda_{i+1}^{(k)} > 0: \quad \varphi_{i+\frac{1}{2}}^{(k)} = \varphi_{i+\frac{1}{2}}^{L,(k)} \quad (20a)$$

$$\text{else if } \lambda_i^{(k)}, \lambda_{i+\frac{1}{2}}^{(k)}, \lambda_{i+1}^{(k)} < 0: \quad \varphi_{i+\frac{1}{2}}^{(k)} = \varphi_{i+\frac{1}{2}}^{R,(k)} \quad (20b)$$

$$\text{else: } \varphi_{i+\frac{1}{2}}^{(k)} = \frac{1}{2} \left(\varphi_{i+\frac{1}{2}}^{L,(k)} + \varphi_{i+\frac{1}{2}}^{R,(k)} \right) - \frac{\lambda_{\max}^{(k)}}{2} \left(\varrho_{i+\frac{1}{2}}^{R,(k)} - \varrho_{i+\frac{1}{2}}^{L,(k)} \right). \quad (20c)$$

Here, $\lambda_{i,i+1,i+\frac{1}{2}}^{(k)}$ are the k th eigenvalue computed at cell centers $i, i+1$ and the Roe-averaged state $\mathbf{U}_{i+\frac{1}{2}}^{Roe}$, and $\varrho_{i+\frac{1}{2}}^{(L,R),(k)}$ are the left- and right-biased characteristic solution components at the interface, computed using the same procedure as described above with

$$\varrho_{(\dots)}^{(k)} = \mathbf{I}^{(k)} \cdot \mathbf{U}_{(\dots)}. \quad (21)$$

Finally, the approximation to the interface flux primitive in Eq. (11) is obtained as

$$\hat{\mathbf{F}}_{i+\frac{1}{2}} = R_{i+\frac{1}{2}} \boldsymbol{\varphi}_{i+\frac{1}{2}}, \quad \boldsymbol{\varphi}_{i+\frac{1}{2}} \equiv [\varphi_{i+\frac{1}{2}}^{(k)} | k = 1, \dots, 4]. \quad (22)$$

This completes the description of the numerical discretization of $\partial_x \mathbf{F}$ and $\partial_y \mathbf{G}$.

The viscous and heat conduction terms on the right-hand side (RHS) of (1), $\partial_x \mathbf{F}_v$ and $\partial_y \mathbf{G}_v$, are dissipative; thus, central differences are used to approximate the spatial derivatives. The fourth-order accurate central finite-difference approximation to the first derivative of a scalar quantity ϕ is given by

$$\frac{\partial \phi}{\partial x} \Big|_i \approx \frac{1}{12} \phi_{i-2} - \frac{2}{3} \phi_{i-1} + \frac{2}{3} \phi_{i+1} - \frac{1}{12} \phi_{i+2}. \quad (23)$$

This is applied component-wise to the calculation of $\partial_x \mathbf{F}_v$ and $\partial_y \mathbf{G}_v$ and the spatial derivatives that appear in Eq. (3). The heat source term, Q_c , corresponds to the heating of the gas by chemical reactions starting from the photoabsorption of ozone in the bright interference fringes in Fig. 2 and is computed by first solving the reaction equations (8) and (9). Since the intensity gradient is mostly along the x axis, the hydrodynamics can be treated independently for each z , and Eq. (1) is only solved in a two-dimensional (x - y) plane that is perpendicular to the beam direction (z). However, Eqs. (8) and (9) are solved on all x - y planes along the beam direction, with the final one being that of the hydrodynamic simulation. This is because the local photon concentration depends on the absorption of photons by reactions along the path of the beam. Let z_h be the z -location of the hydrodynamic simulation plane, and let $[0, z_h]$ be discretized by N_z points. The photon concentration at $z = 0$ corresponds to that of the incident beam; at subsequent z -locations, the photon concentration is solved at each grid point (i, j) by discretizing (9) with the forward Euler method

$$[h_\nu]_l = [h_\nu]_{l-1} + \Delta z \sigma [h_\nu]_{l-1} [O_3]_{l-1}, \quad 1 \leq l \leq N_z. \quad (24)$$

The reaction ordinary differential equations (ODEs) (8) are then solved locally at each x - y grid point on each z -plane with the classical fourth-order, four-stage Runge–Kutta (RK4) method. Finally, Q_c is calculated at each grid point on the hydrodynamic simulation plane with (10).

The spatially discretized form of (1) is a system of ordinary differential equations (ODEs) that is evolved in time with the RK4 method. The time step, Δt , is chosen based on the CFL stability condition.

III. INVESTIGATION OF THE NONLINEAR HYDRODYNAMICS REGIME OF GAS OPTICS

In the following, we will use the code in 1D only, with x the direction of the UV modulation (cf. Fig. 2). This is appropriate for the study of gratings (which are 1D structures) and allows a direct comparison with the model from Ref. 9 based on the analytical solution of the 1D linearized hydro equations. We will also restrict our discussion to the situation where the duration of the UV imprint beam is much shorter than the acoustic period, although the code is capable of modeling UV pulses with durations longer than the acoustic period.

A. Validation of the linear theory

In this first section, we aim to validate the linear theory derived in Ref. 9. The comparison between the density perturbation resulting from the same initial heating is represented in Fig. 3. These simulations are performed without damping, and periodic boundary conditions are applied along the x -direction. The period of the grating is

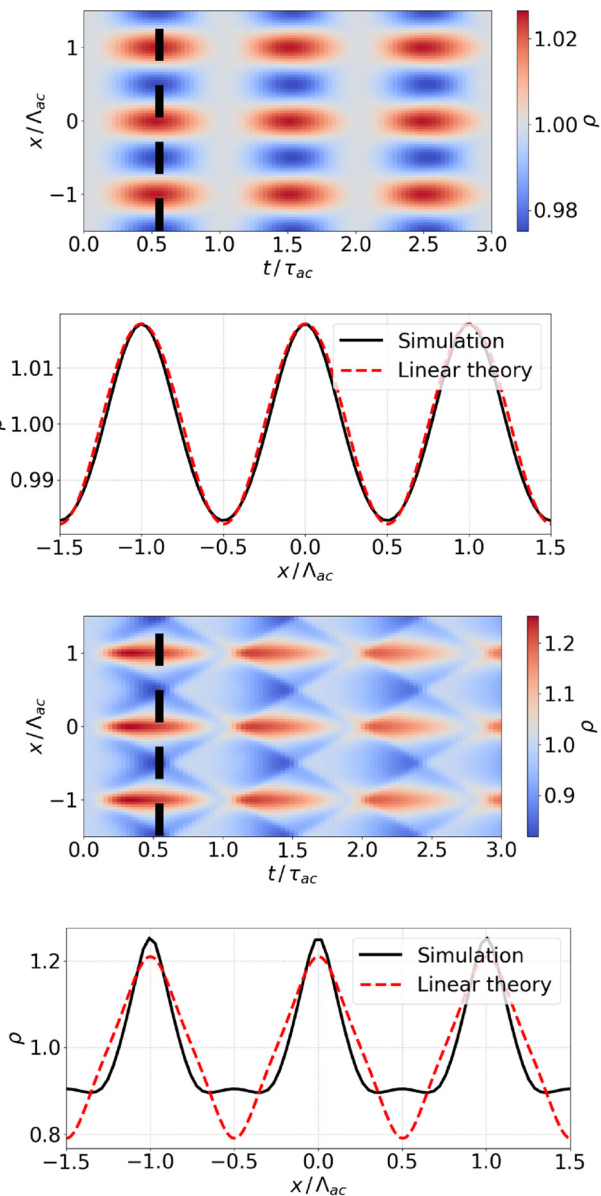


FIG. 3. Density perturbation initiated by laser heating: (a) vs x and t for a 2% initial perturbation and (b) lineout at the time of the first maximum of the density modulation [dashed line on (a)]. (c) and (d) Same as (a) and (b) for a 20% initial perturbation. The linear case parameters (a) and (b) are $[O_3] = 0.5\%$, UV fluence = 10 mJ/cm^2 , corresponding to $\Delta T_{\max}/T_0 = 0.03$; and for the nonlinear case (c) and (d): $[O_3] = 1.5\%$, UV fluence = 100 mJ/cm^2 , corresponding to $\Delta T_{\max}/T_0 = 0.35$.

$\Lambda_{ac} = 42 \mu\text{m}$, the acoustic period is defined as $\tau_{ac} = \Lambda_{ac}/c = 130 \text{ ns}$ and the laser pulse duration is $\tau_{pulse} = 10 \text{ ns}$. The lineout of the density modulation along x is plotted at the time when it reaches its maximum for the linear theory (red dotted lines) and the simulation (dark line). The agreement is excellent for a small perturbation (2%); a discrepancy becomes visible for a stronger perturbation (20%), but the agreement remains acceptable.

Although the linear theory remains reasonably consistent with the 20% simulation perturbation around half of the first period, the $x-t$ map indicates that nonlinearity increases over time. The modification of the wave shape during its propagation will be addressed in the following Section III B.

B. Nonlinear behavior of the acoustic wave

In Ref. 9, we show that the density perturbation is the sum of an entropy wave and a standing acoustic wave (which is itself the sum of two counter-propagating acoustic waves). In the linear regime and for times much smaller than the entropy and acoustic modes' damping times, both waves contribute equally to the density modulation. However, an entropy wave and an acoustic wave have fundamentally

different behaviors in the nonlinear regime. For an acoustic wave, the nonlinear $(\mathbf{v} \cdot \nabla)\mathbf{v}$ term in the fluid momentum equation implies that the velocity of the fluid elements at the crest of the pressure perturbation is higher than for those at the bottom of the perturbation, which leads to a steepening of the wave profile and ultimately to the well-known sawtooth profile illustrated in Fig. 4.²¹ The “time to shock,” i.e., the time required to get to the sawtooth profile (leading to a shock in the absence of dissipation), is simply the time needed for the fluid elements at the crest of the perturbation to catch up with the fluid elements at the bottom, $t_{shock} = \Lambda_{ac}/4\delta v$, with δv the half-amplitude of the velocity perturbation of the acoustic wave. The velocity perturbation can be expressed as a function of the pressure perturbation and initial density as $\delta v = \pm \delta p/\rho_0 c$,⁹ which leads to

$$t_{shock} = \frac{\Lambda_{ac}\rho_0 c}{4\delta p}. \quad (25)$$

In the absence of damping, the standing wave generated by a sinusoidal perturbation at $t = 0$ evolves to a square shape at $t = t_{shock}$ (sum of two sawtooth waves), as illustrated in Fig. 4.

The steepening of the wave leads to the generation of higher-order Fourier modes for the wave's spatial profile

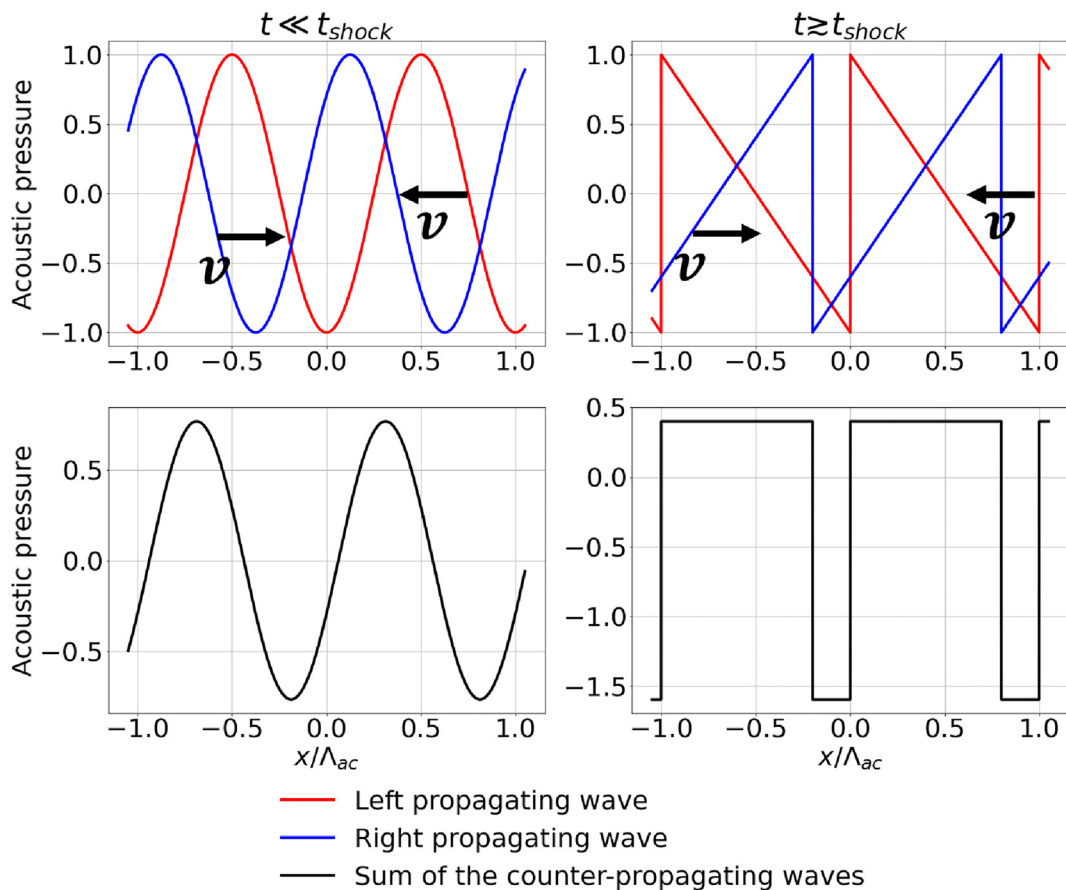


FIG. 4. Illustration of the time evolution of a standing acoustic wave via its counter-propagating components at times long before the steepening ($t \ll t_{shock}$) and after the shock ($t \geq t_{shock}$). The standing wave evolves toward a square profile.

$$\Delta n(x, z, t) = \sum_{m=-\infty}^{\infty} n_m(z, t) \exp[imKx], \quad (26)$$

$$n_m(z, t) = \frac{1}{\Lambda} \int_0^{\Lambda} \Delta n(x, z, t) \exp[-imKx] dx, \quad (27)$$

with $K = 2\pi/\Lambda$, and to the transfer of energy from the fundamental sinusoidal mode ($|m| = 1$) to the higher-order modes.

On the other hand, since the entropy mode is not associated with a pressure perturbation and does not propagate, no steepening occurs and the spatial frequency spectrum is not affected. This difference will impact the damping of the two types of waves under conditions of strong, nonlinear excitation by the gas heating, as shown in the Sec. III C.

C. Linear/nonlinear damping

To investigate the differences in dissipation between acoustic and entropy modes, we first study the evolution of a pure acoustic wave vs a pure entropy mode in the code. This is obtained by appropriately defining the initial conditions.

1. Damping of the acoustic wave

For the acoustic wave, the initial conditions are

$$\begin{aligned} \rho(x, t=0) &= \rho_0 + \delta\rho \cos Kx, \\ p(x, t=0) &= p_0[1 + \gamma\delta\rho/\rho_0 \cos Kx]. \end{aligned} \quad (28)$$

This corresponds to an adiabatic situation, where the entropy is not modified at $t = 0$ (indeed, $ds = c_v[d\rho/p - \gamma d\rho/\rho] = 0$). This initial condition initiates two counter-propagating acoustic waves, as in the Sec. III C, but without the entropy mode.

The linear damping rate for the acoustic wave is

$$\nu_{ac} = \frac{K^2}{2\rho_0} \left(\frac{4}{3}\mu + \frac{\kappa}{C_p}(\gamma - 1) \right), \quad (29)$$

where μ is the viscosity and κ the heat conduction.²¹

The x - t maps of the density for a linear ($\delta\rho/\rho = 1\%$) and nonlinear ($\delta\rho/\rho = 50\%$) excitation at $t = 0$ are shown in Fig. 5.

With 1% initial perturbation amplitude, the wave remains sinusoidal for many acoustic periods and dampens before steepening. On the other hand, in the nonlinear case the steepening of the wave is visible at the very beginning of the simulation, before even half an acoustic period. The nonlinearity develops well before the wave is damped. The other noticeable feature is that the nonlinear wave damps much faster than in the linear case.

This different behavior in the nonlinear vs linear case (profile steepening and increased damping) can be explained and quantified by considering the ratio of the time to shock to the acoustic damping time, $\Gamma = t_{shock}\nu_{ac}$. If $\Gamma > 1$, the fundamental mode will damp before any profile steepening can occur. On the other hand, for $\Gamma < 1$, higher-order modes (i.e., wave steepening) develop before the fundamental mode has damped. Furthermore, the damping of a higher-order mode m is m^2 times faster than the fundamental per Eq. (29); therefore, since profile steepening corresponds to a transfer of energy from the fundamental to the higher-order modes, the overall damping of the acoustic wave can greatly exceed the damping of the initial perturbation at $m = 1$ when $\Gamma < 1$.

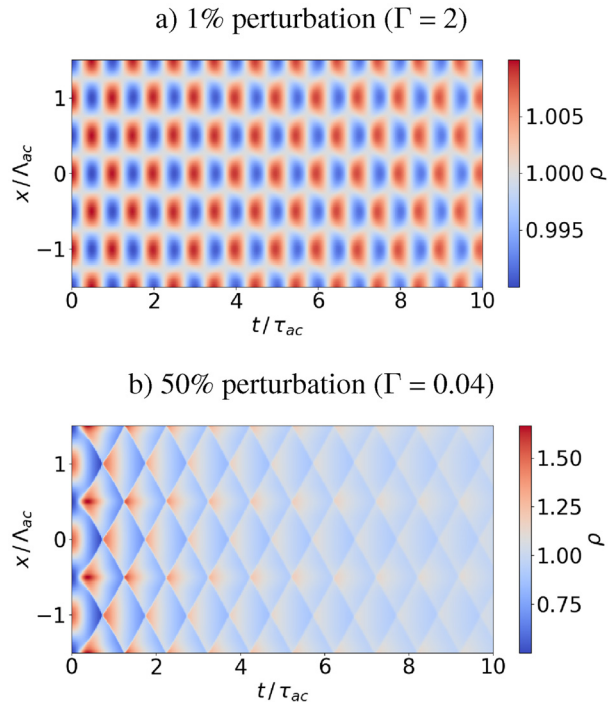


FIG. 5. x - t maps of the density of a purely acoustic wave: (a) the linear regime (1% modulation) and (b) the nonlinear regime (50% modulation).

Using $t_{shock} = \Lambda_{ac}/4\delta v = \pi/2K\delta v$ as defined in the Sec. III C1, the criterion for this nonlinear behavior can be expressed as

$$\Gamma = t_{shock}\nu_{ac} = \frac{\pi^2 \rho_0 c}{2\Lambda_{ac}\delta p} \left[\frac{4}{3}\mu + \frac{\kappa}{C_p}(\gamma - 1) \right]. \quad (30)$$

For the typical values $c = 324 \text{ m s}^{-1}$, $\lambda = 42 \mu\text{m}$, $\nu = 1.8 \times 10^{-5} \text{ kg s}^{-1} \text{ m}^{-1}$, $\kappa = 2.5 \times 10^{-2} \text{ W m}^{-1} \text{ K}^{-1}$, $C_p = 918$, $\gamma = 7/5$, we obtain $\Gamma = 2$ if $\delta p_1/p = 1\%$ and $\Gamma = 0.04$ if $\delta p_1/p = 50\%$ (the two values used in Fig. 5).

Figure 6 shows the relative shape of the acoustic pressure and the density modulation for the same two initial perturbations. The density modulation corresponds to a lineout of Fig. 5 at $t \approx 3\tau_{ac}$. The pressure perturbation is sinusoidal in the linear case, and in the nonlinear case, takes the shape of a square wave as was already illustrated and discussed in Fig. 4.

Figure 7 shows the evolution of the density modulation as a function of time, corresponding to the lineouts at $x = 0$ of Fig. 5. The “mode 1” damping corresponds to $e^{-\nu_{ac}t}$ where ν_{ac} is defined in Eq. (29). For $\Gamma = 2$, the acoustic wave of the simulation follows the theoretical mode 1 damping. For $\Gamma = 0.04$, the energy transfer to higher-order modes leads to a faster, nonlinear damping.

2. Damping of the entropy wave

To initialize a pure entropy wave, we use the following initial conditions:

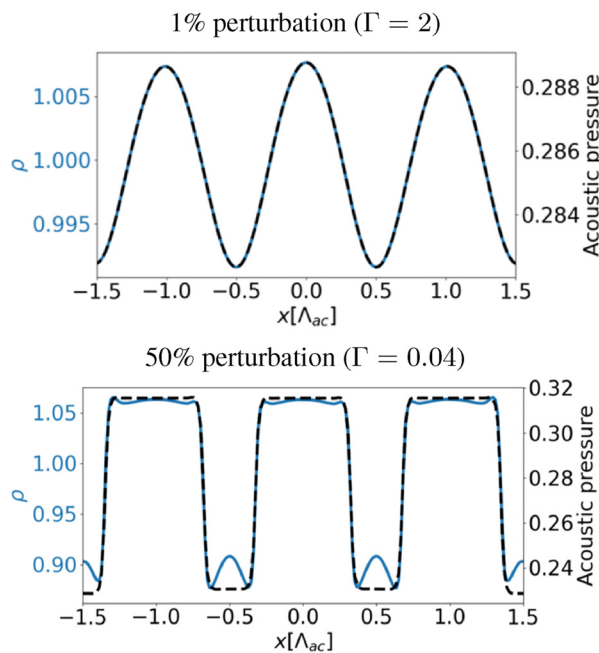


FIG. 6. Lineout of the density and the acoustic pressure from Fig. 5 at $t \approx 3\tau_{ac}$.

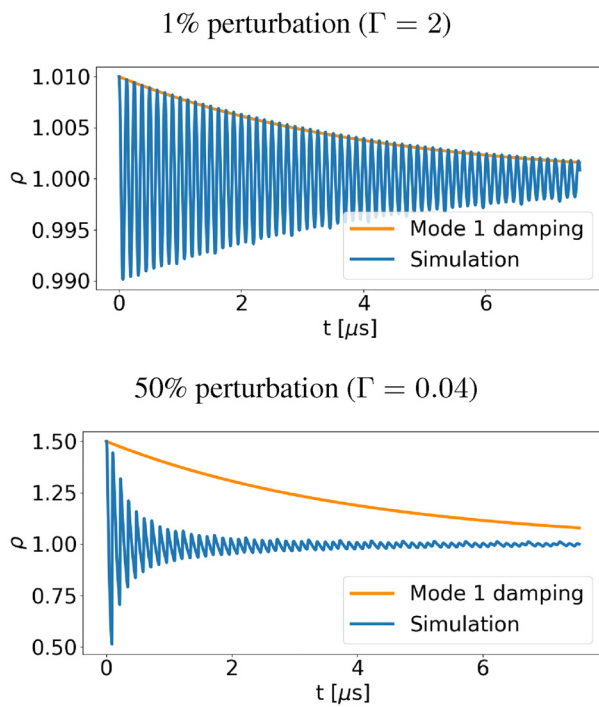


FIG. 7. Evolution of the density perturbation amplitude of a purely acoustic wave as a function of time, from Fig. 5 at $x = 0$, for an initial perturbation of 1% ($\Gamma = 2$) and 50% ($\Gamma = 0.04$).

$$\begin{aligned} \rho(x, t=0) &= \rho_0 + \delta\rho \cos Kx, \\ p(x, t=0) &= p_0. \end{aligned} \quad (31)$$

Because it is not associated with a pressure perturbation, this density modulation is accompanied by a corresponding entropy modulation $\delta s(x, t=0) = -\gamma(\delta\rho/\rho_0) \cos(Kx)$ and temperature modulation $\delta T/T_0 = -\delta\rho/\rho_0$.

The linear damping rate for the entropy wave is given by²¹

$$\nu_{en} = \frac{\kappa K^2}{\rho C_p}. \quad (32)$$

While the acoustic wave is damped by both thermal diffusion and viscosity, the entropy wave is not propagating and therefore not affected by viscosity. Furthermore, since the entropy mode does not propagate, no steepening (i.e., energy transfer to higher-order spatial mode) occurs, and the damping is not significantly impacted by the amplitude of the initial density perturbation. This has been verified by simulations shown in Fig. 8, where a pure entropy mode was initialized with initial density modulation amplitudes of 1% and 50%.

Figure 9 shows the evolution of the density modulation as a function of time, from Fig. 8 at $x = 0$. The “mode 1” damping corresponds to $e^{-\nu_{ent}t}$ where ν_{ent} is defined in Eq. (32). It confirms that unlike for a standing acoustic wave, the damping of an entropy mode is largely unaffected by the initial amplitude of the density perturbation. This different behavior between the two modes will lead to significantly different temporal behaviors of the gas optics depending on the initial amplitude of the gas heating, as discussed in the Sec. III C3.

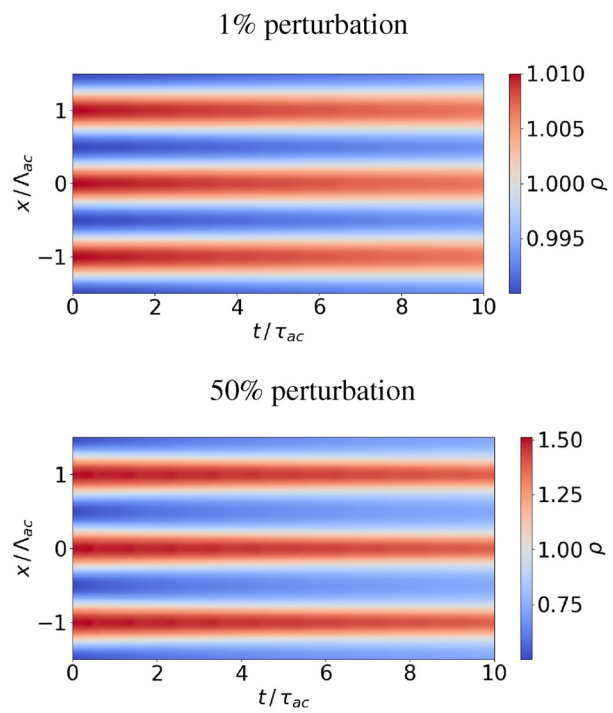


FIG. 8. x - t maps of the density of an entropy wave for 1% and 50% initial amplitudes for the density perturbation.

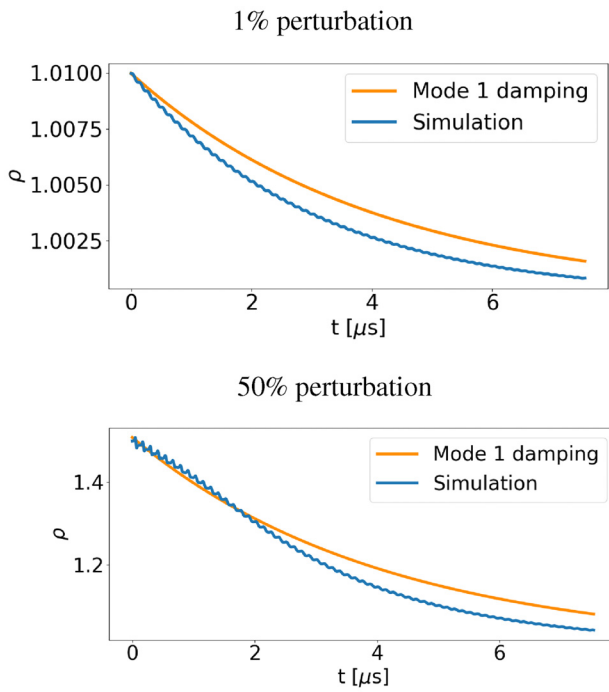


FIG. 9. Evolution of the density perturbation amplitude of an entropy wave as a function of time, at $x = 0$, for an initial perturbation of 1% vs 50%.

3. Damping of a chemically induced wave and calculation of diffraction efficiency

The damping is now studied in a situation relevant to gas optics, where the gas heating launches both an acoustic and an entropy mode of equal amplitudes at $t = 0$. The period of the grating and UV laser pulse duration are the same as in the Sec. III C2 (42 μm and 10 ns, respectively). The gas length is $L = 3 \text{ mm}$ (cf. Fig. 2); since the gradients are much larger along x than along z , we still assume 1D hydrodynamics in the following and run multiple 1D simulations for various z accounting for UV absorption and ozone depletion along z .

In the linear case the imprint laser fluence is 5 mJ/cm^2 , and the ozone concentration is 0.5%. This initiates a perturbation of $\approx 1\%$ amplitude as seen in Fig. 10, with a corresponding $\Gamma = 2$ from Eq. (30). For the nonlinear case, the laser fluence is 120 mJ/cm^2 and the ozone concentration is 2%, initiating a perturbation of $\approx 40\%$ amplitude and $\Gamma = 0.05$.

For low fluence/ozone concentration, the wave remains linear and is slowly damped over time. The sinusoidal pattern is still discernible at the end of the simulation. For high fluence/ozone concentration, the steepening of the wave is noticeable at the very beginning of the simulation, and the damping is strong after the first few oscillations.

We now assume that a diffracted beam with wavelength $\lambda_d = 266 \text{ nm}$ is incident on the grating at the Bragg angle and calculate the diffraction efficiency. Note that the diffracted beam's wavelength is within the ozone absorption band, but if its fluence is much larger than the saturation fluence, which would be the case for high-energy laser applications, ozone will be fully depleted and the diffracted beam's absorption will become negligible—as was recently confirmed

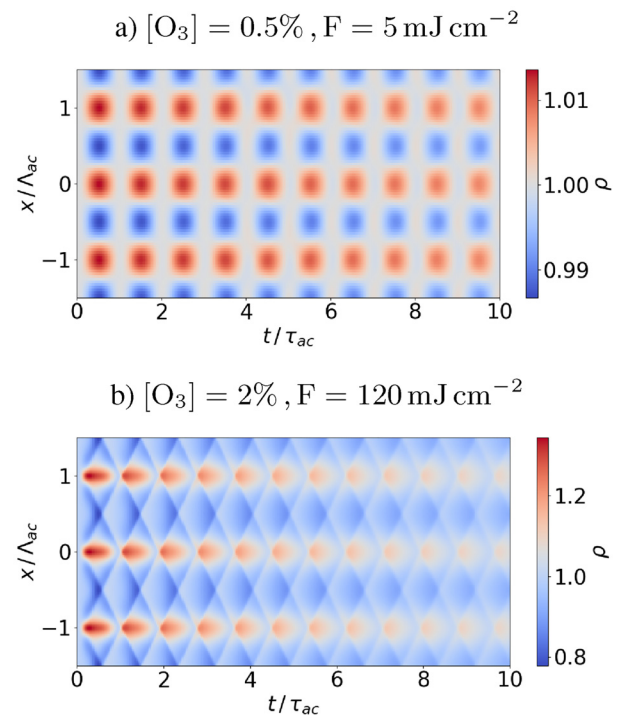


FIG. 10. x - t maps of the density of a wave composed of an entropy and an acoustic mode in (a) the linear regime and (b) the nonlinear regime.

experimentally.²² The diffraction efficiency of the grating is related to the density modulation's first mode of the Fourier series,⁹ leading to

$$\eta(z) = \sin^2 \left(\frac{k_d}{2n_0} \int_0^z n_1(z') dz' \right), \quad (33)$$

where n_1 is first mode of the refractive index n and $k_d = 2\pi/\lambda_d$ is the diffracted beam's wavenumber.

The diffraction efficiency of the grating as a function of time is plotted in Fig. 11. In the linear case [Fig. 11(a)], the diffraction efficiency oscillates at the acoustic period and returns to zero at each oscillation. On the other hand, in the nonlinear case [Fig. 11(b)], the diffraction does not return to zero at each oscillation, and the temporal oscillations damp over approximately 1 μs while some diffraction still remains, at $\approx 25\%$ efficiency—which means that a grating still exists, but not an oscillating one. This is a signature of the different damping between the acoustic and entropy modes. The entropy wave, which damps more slowly than the acoustic wave as discussed above, continues to diffract the probe laser beam.

Another apparent difference between the two cases is the “dip” in diffraction efficiency in the first three periods of Fig. 11. This is a signature of the gas grating operating past the 100% efficiency optimum. Indeed, for transmission gratings, 100% diffraction efficiency is obtained when $\delta n_{opt}/n = \lambda_d/2L$, where δn_{opt} is the (optimum) index modulation (assumed constant along the propagation direction in this formula), λ_d the diffracted beam wavelength, and L the grating thickness.²³ When the index modulation increases past δn_{opt} while L is kept fixed, the diffraction efficiency goes back down. It is the same process

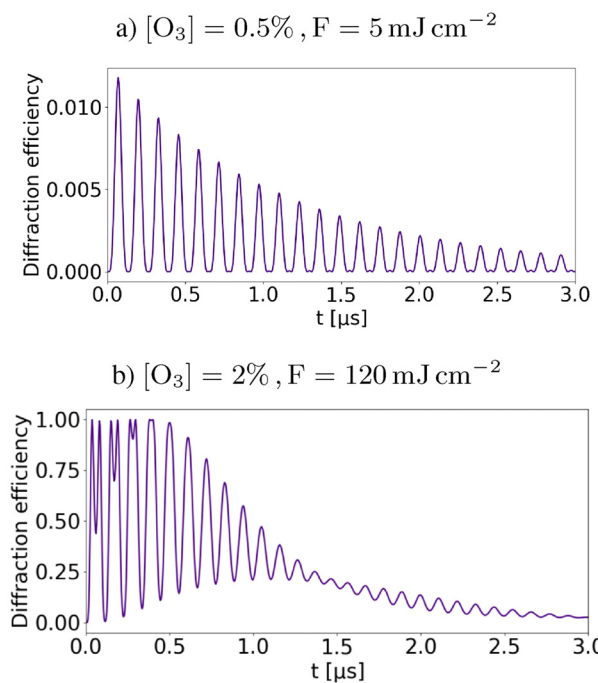


FIG. 11. Evolution of diffraction efficiency of a chemically induced grating as a function of time, at $x = 0$.

at the origin of the “roll-over” in the theoretical curves of diffraction efficiency vs UV fluence in Ref. 9. Here, the “dip” appears because the index modulation from the wave is still increasing when the efficiency has already reached 100%, which leads to the efficiency dropping back down until the density (thus index) modulation amplitude has reached its peak; the process then reverses.

All these features (“hump” from the entropy wave in the nonlinear regime of acoustic damping and “dip” in the first few oscillations of the diffraction efficiency) have been observed in recent experiments;²² these results will be published separately.

IV. CONCLUSION

We have developed a hydrodynamics code that combines the coupled evolution of chemical processes and nonlinear hydrodynamic behavior. For linear situations, we were able to confirm the theoretical model developed in our previous paper.⁹ The code allowed us to develop a quantitative understanding of the waves involved in gas optics in the nonlinear hydrodynamics regime. This code will be used for the design of future experiments aimed at demonstrating the applications of gas optics for the manipulation of high-energy lasers and for the development of gaseous diffractive elements beyond simple gratings (e.g., chirped gratings or diffractive lenses).

ACKNOWLEDGMENTS

Work performed under the auspices of the U.S. Department of Energy by Lawrence Livermore National Laboratory under Contract DE-AC52-07NA27344 and funded by the Laboratory Research and Development Program at LLNL under Project Tracking Code No.

24-ERD-001. C.R. acknowledges financial support from the Fédération de Recherche Plasmas à Paris—PLAS@PAR.

AUTHOR DECLARATIONS

Conflict of Interest

The authors have no conflicts to disclose.

Author Contributions

A. Oudin: Conceptualization (equal); Formal analysis (equal); Investigation (equal); Software (equal); Visualization (lead); Writing – original draft (lead). **D. Ghosh:** Software (equal); Writing – original draft (supporting). **C. Riconda:** Investigation (equal); Writing – review & editing (supporting). **L. Lancia:** Investigation (equal). **E. Kur:** Investigation (supporting). **K. Ou:** Investigation (supporting). **V. M. Perez-Ramirez:** Investigation (supporting). **J. Lee:** Investigation (supporting). **M. R. Edwards:** Investigation (supporting); Supervision (supporting); Writing – review & editing (supporting). **P. Michel:** Conceptualization (equal); Formal analysis (equal); Funding acquisition (lead); Investigation (equal); Supervision (lead); Visualization (supporting); Writing – review & editing (lead).

DATA AVAILABILITY

The data that support the findings of this study are available from the corresponding author upon reasonable request.

REFERENCES

- ¹Basic Research Needs Workshop on Inertial Fusion Energy, “Report of the fusion energy sciences workshop on inertial fusion energy,” Technical Report (Fusion Energy Sciences Team, U.S. Department of Energy, 2022).
- ²H. Abu-Shwareb *et al.*, *Phys. Rev. Lett.* **129**, 075001 (2022).
- ³H. Abu-Shwareb *et al.*, *Phys. Rev. Lett.* **132**, 065102 (2024).
- ⁴R. Moir, *Fusion Eng. Des.* **51–52**, 1121 (2000).
- ⁵G. Lehmann and K.-H. Spatschek, *Phys. Rev. Lett.* **116**, 225002 (2016).
- ⁶M. R. Edwards *et al.*, *Phys. Rev. Lett.* **133**, 155101 (2024).
- ⁷Y. Michine and H. Yoneda, *Commun. Phys.* **3**, 24 (2020).
- ⁸Y. Michine, R. M. More, and H. Yoneda, *Phys. Fluids* **36**, 041703 (2024).
- ⁹P. Michel *et al.*, *Phys. Rev. Appl.* **22**, 024014 (2024).
- ¹⁰M. Thelen, T. Gejo, J. A. Harrison, and J. R. Huber, *J. Chem. Phys.* **103**, 7946 (1995).
- ¹¹M. J. Daniels and J. R. Wiesenfeld, *J. Chem. Phys.* **98**, 321 (1993).
- ¹²G.-S. Jiang and C.-W. Shu, *J. Comput. Phys.* **126**, 202 (1996).
- ¹³J. Burkholder *et al.*, “Chemical kinetics and photochemical data for use in atmospheric studies; evaluation number 19,” Technical Report (Jet Propulsion Laboratory, National Aeronautics and Space, Pasadena, CA, 2020).
- ¹⁴J. Green, J. Shi, and J. Barker, *J. Phys. Chem. A* **104**, 6218 (2000).
- ¹⁵C. Hirsch, *Numerical Computation of Internal and External Flows: The Fundamentals of Computational Fluid Dynamics* (Elsevier Science, 2007), Vol. 1 and 2.
- ¹⁶J. Hilsenrath, *Tables of Thermal Properties of Gases: Comprising Tables of Thermodynamic and Transport Properties of Air, Argon, Carbon Dioxide, Carbon Monoxide, Hydrogen, Nitrogen, Oxygen, and Steam* (US Department of Commerce, National Bureau of Standards, 1955), Vol. 564.
- ¹⁷H. S. Johnston, *Annu. Rev. Phys. Chem.* **43**(1), 1 (1992).
- ¹⁸C.-W. Shu and S. Osher, *J. Comput. Phys.* **77**, 439 (1988).
- ¹⁹C.-W. Shu and S. Osher, *J. Comput. Phys.* **83**, 32 (1989).
- ²⁰C. B. Laney, *Computational Gasdynamics* (Cambridge University Press, 1998).
- ²¹A. D. Pierce, *Acoustics: An Introduction to Its Physical Principles and Applications* (Springer, 2019).
- ²²K. Ou *et al.*, “Experimental characterization of photochemically induced gas gratings” (unpublished).
- ²³R. W. Boyd, *Nonlinear Optics*, 3rd ed. (Academic Press, Inc., Orlando, FL, 2008).